*polysaccharides*

MDPI

*Article*

# Synthesis and Characterization of Self-Assembled Highly Stearate-Grafted Hydroxyethyl Starch Conjugates

**Rana Hore [1], Haroon Rashid [1,2], Frank Syrowatka [3] and Jörg Kressler [1,*]**

[1] Department of Chemistry, Martin Luther University Halle-Wittenberg, Von-Danckelmann-Platz 4, D-06099 Halle/Saale, Germany; rana.hore@chemie.uni-halle.de (R.H.); haroon.rashid@student.uni-halle.de (H.R.)
[2] Department of Pharmacy, Martin Luther University Halle-Wittenberg, Weinbergweg 22, D-06120 Halle/Saale, Germany
[3] Interdisciplinary Center of Materials Science, Martin Luther University Halle-Wittenberg, Heinrich-Damerow-Str. 4, D-06120 Halle/Saale, Germany; frank.syrowatka@cmat.uni-halle.de
* Correspondence: joerg.kressler@chemie.uni-halle.de

**Abstract:** Polysaccharide-based nanoformulations with tailored hydrophobic properties have become a frontier in nanomedicine applications. Herein, highly hydrophobicized hydroxyethyl starch (HES) conjugates were synthesized by grafting stearic acid (SA) with HES via a carbodiimide-mediated reaction. A detailed NMR characterization of HES and the conjugates was studied to obtain structural information. The grafting ratio of the stearate-HES (St-HES) conjugates was determined from $^1$H NMR spectra as 29.4% (St-HES29.4) and 60.3% (St-HES60.3). Thermal analyses and X-ray diffractograms suggested an entire transition from amorphous HES to a semicrystalline (St-HES60.3) character upon increasing the degree of grafting. Both conjugates, St-HES29.4 and St-HES60.3, were able to form self-assembled particles with a diameter of 130.7 nm and 152.5 nm, respectively. SEM images showed that the self-aggregates were mostly spherical in shape. These conjugates can be employed to entrap highly hydrophobic drugs with an increased encapsulation efficiency and loading capacity.

**Keywords:** polysaccharide; 1D and 2D NMR spectroscopy; hydrophobicized hydroxyethyl starch; St-HES; self-aggregates



**Citation:** Hore, R.; Rashid, H.; Syrowatka, F.; Kressler, J. Synthesis and Characterization of Self-Assembled Highly Stearate-Grafted Hydroxyethyl Starch Conjugates. *Polysaccharides* **2024**, *5*, 142–157. https://doi.org/10.3390/polysaccharides5020011

Academic Editor: Karin Stana Kleinschek

Received: 26 March 2024
Revised: 24 April 2024
Accepted: 31 May 2024
Published: 5 June 2024



## 1. Introduction

During the past decades, polymeric amphiphiles have received extensive attention owing to their distinctive properties and potential applications in the pharmaceutical and biomedical fields [1]. Such amphiphilic polymers have a unique supramolecular core–shell-like structure that can self-assemble in an aqueous environment to form polymeric nanoparticles or micelles, a promising drug delivery system to enhance bioavailability, and deliver hydrophobic bioactive materials with a better solubility profile [2]. The hydrophobic inner compartment serves as a microdomain for encapsulating various hydrophobic drugs and the outer hydrophilic corona provides steric stabilization, which can enhance the blood circulation time of the micelles and preserve active ingredients from rapid degradation [3–5]. The critical micelle concentration (CMC) is an important parameter to access the behavior of micelles. Amphiphilic molecules form micelles when concentration is at or above CMC. However, when administered in vivo, conventional micellar systems may encounter dilution effects below CMC in the bloodstream which may lead to the dissociation of micelles and premature drug release [6]. Several crosslinking and non-crosslinking approaches have been utilized to lower CMC and improve the stability of polymeric micelles. One of the strategies to lower the CMC is to increase the hydrophobic block and alter the crystallinity of the hydrophobic core of the micelles. Increasing the hydrophobic segments may enhance the hydrophobic interactions and the crystallization process may serve as an additional driving force for micelle assembly, consequently leading to a decreased CMC value [6,7].

Generally, the self-aggregates or micelles can be fabricated from macromolecular self-assembly using both synthetic and natural polymers. Biodegradability and biocompatibility are the most essential properties for the development of nanoparticulated polymer-based drug delivery systems [8]. Numerous polymeric amphiphiles have been studied as potential carriers for drug delivery systems and some of them are already available for commercial use [9]. Among them, synthetic polymers have played an essential role in the design and development of carrier systems for drug delivery. However, there are safety issues regarding their immunogenicity, non-biodegradability, and non-renewable sources [10]. Hence, natural biopolymers and their derivatives have gained particular research interest due to their versatility, unique properties, and available natural resources [11]. Polysaccharides, one of the most important and diverse classes of natural biopolymers, have been widely recognized and applied in biotechnology and biomedical applications. Moreover, natural polysaccharides have been notably studied as drug carriers due to their versatile characteristics such as wide accessibility, biocompatibility, biodegradability, and structural diversity [12]. In order to impart amphiphilicity, molecular modification is necessary to tailor their structures that can construct self-assembled nanocarriers for drug delivery [13]. Over the years, several polysaccharides and their derivatives have been investigated and studied as a potent carrier for drugs [14].

Hydroxyethyl starch (HES) is a semisynthetic derivative of starch utilized globally as a plasma volume expander [15]. In addition, HES attracts considerable interest as a designed nanocarrier in the form of nanomedicines due to its excellent properties such as biocompatibility, biodegradability, and low immunogenicity [16,17]. Moreover, introducing hydroxyethyl groups to the starch backbone in HES increases the water solubility of starch and improves stability to hydrolysis in vivo [18,19] making it one of the most favorable alternatives to fabricate nanocarriers in the pharmaceutical field. HESylation® is an excellent half-life extension (HLE) strategy to improve pharmacokinetic and pharmacodynamic properties based on the conjugation of HES with biopharmaceuticals [20,21]. However, several studies revealed an increased risk of kidney injury or renal dysfunction when HES is administered particularly to critically ill patients with sepsis requiring fluid resuscitation [22]. It is noteworthy that HES is used in substantially lower concentrations for nanoparticle preparation compared to fluid resuscitation therapy, therefore, safety concerns associated with HES are significantly reduced. Accordingly, various HES-based prodrugs, bioconjugates, nanocarriers, and hydrogels have been studied for the delivery of drugs and biomacromolecules [23]. For example, recently we reported an enzymatic approach for the conjugation of HES with recombinant human erythropoietin (HES-rHuEPO) via thermoresistant variant microbial transglutaminase, $TG^{16}$ [24]. Accordingly, long-chain fatty acids have been used to obtain hydrophobically modified HES which can form self-assembled nanoparticles in aqueous media. Among them, HES modified with a low degree of grafting formed stable nanodispersions [25,26]. Stearic acid (SA) is a naturally occurring long-chain fatty acid widely used as a pharmaceutical excipient. Furthermore, SA has been explored in the field of polymeric nanoparticle formulations for drug delivery due to its better biocompatibility with low toxicity [27]. It was observed that a higher grafting ratio of SA may lead to an increased amount of drug loading [28].

Based on these considerations, highly grafted fatty acid esters of HES have been investigated by introducing stearate side chains for the preparation of polymeric self-aggregates to attain high encapsulation efficiency and sustained release of drugs or therapeutics. Initially, SA was covalently attached to HES via an esterification reaction to synthesize stearate-HES (St-HES) conjugates. Detailed structural and physicochemical characteristics of the native HES and two different grafted St-HES conjugates were thoroughly investigated by $^{1}$H NMR, 2D heteronuclear single quantum coherence (HSQC), and heteronuclear multiple bond correlation (HMBC) spectroscopy, differential scanning calorimetry (DSC) and wide-angle X-ray scattering (WAXS). Afterwards, the synthesized conjugates were used to prepare self-assembled micelles in an aqueous phase. The particle size and mor-

phology of the micelles were characterized by dynamic light scattering (DLS) and scanning electron microscopy (SEM).

## 2. Materials and Methods

### *2.1. Materials*

Hydroxyethyl starch (HES) with a weight average molar mass ($M_w$) of 70 kDa and molar substitution (the number of hydroxyethyl residues per glucose subunit) of 0.5 was a gift from Serumwerk Bernburg, Germany. Stearic acid was obtained from Sigma-Aldrich (Steinheim, Germany). N,N-dimethylformamide (DMF, extra dry, 99.8%) was purchased from Acros Organics (Schwerte, Germany). Tetrahydrofuran (THF), 4-(dimethylamino)pyridine (DMAP), 1-ethyl-3-(3-dimethylaminopropyl)carbodiimide hydrochloride (EDC·HCl), dimethyl sulfoxide (DMSO), and dialysis membrane (having a cut-off molar mass of 3000 g/mol) were purchased from Carl Roth (Karlsruhe, Germany). N,N-dimethylformamide-$d_7$ (DMF-$d_7$, 99.5%), dimethyl sulfoxide-$d_6$ (DMSO-$d_6$, 99.8%), and deuterium oxide ($D_2O$, 99.9%) were purchased from Armar Chemicals (Döttingen, Switzerland). Ethanol and diethyl ether were reagent grade and used as received.

### *2.2. Methods*

#### 2.2.1. Nuclear Magnetic Resonance (NMR) Spectroscopy

The NMR spectra were acquired on a VNMRS spectrometer (Agilent Technologies, Santa Clara, CA, USA) at 500 MHz for $^1$H and 125 MHz for $^{13}$C and the attached proton test (APT) $^{13}$C NMR measurements. Two-dimensional (2D) NMR measurements, namely, HSQC and HMBC spectroscopy, were performed for complete structural characterization. For native HES, 20 mg of samples were dissolved in 0.6 mL of deuterated solvents and the measurements were carried out at 27 °C using tetramethylsilane (TMS) as an internal standard. For synthesized St-HES conjugates, 2–10 mg of samples were dissolved in 0.6 mL of deuterated solvents at 50 °C for complete dissolution and the measurements were carried out at 50 °C using TMS standard. The residual solvent signals were set for DMSO-$d_6$ at $\delta_H$ 2.50 ppm and $\delta_C$ 39.52 ppm, for $D_2O$ at $\delta_H$ 4.79 ppm, and for DMF-$d_7$ at $\delta_H$ 2.75, 2.92 and 8.03 ppm. An intense residual HDO peak was observed in the NMR spectra, which may be due to the hygroscopic nature of both NMR solvents and HES. The NMR spectral data were interpreted using MestRec (v.4.9.9.6) software (Mestrelab Research, Santiago de Compostela, Spain).

#### 2.2.2. Differential Scanning Calorimetry (DSC)

DSC measurements were carried out using a Mettler Toledo DSC 822$^e$ (Schwerzenbach, Switzerland) instrument. A total of 4–5 mg of the samples was poured into 40 µL aluminium pans and then sealed. The experiments were run in a temperature range from −60 °C to 120 °C with a heating and cooling rate of 1 K/min, a holding time of 10 min, and a continuous nitrogen flow of 10 mL/min. All DSC data were taken from the second heating curve.

#### 2.2.3. Wide-Angle X-ray Scattering (WAXS)

The wide-angle X-ray diffraction patterns were recorded with a PANalytical Empyrean Diffractometer. The instrument was equipped with a position-sensitive PIXcel-3D detector in Bragg–Brentano geometry. The samples were measured on a silicon zero-background substrate in a TTK 450 temperature chamber (Anton Paar) with Ni-filtered $CuK_\alpha$ ($\lambda$ = 0.15418 nm) radiation. The measurements were performed under a constant nitrogen flow. The diffractograms were recorded with a scattering angle of 2$\theta$ in the range of 6° to 60° with a step size of 2$\theta$ = 0.053° and a counting time of 93 s per step. The samples were initially heated to 100 °C and then cooled to T = −30 °C with a cooling rate of 10 K/min. All the WAXS diffractograms were recorded at T = −30 °C, except SA, which was recorded at room temperature.

2.2.4. Determination of Particle Size by Dynamic Light Scattering (DLS)

The particle size and intensity-weighted size distribution of the self-aggregates were determined by DLS using a Litesizer 500 device (Anton Paar GmbH, Graz, Austria) at 25 °C. The sample concentration of 0.1 mg/mL in water was taken in 70 µL micro cuvettes and measured at a light wavelength of 658 nm and a detection angle of 175°. Hydrodynamic diameter ($D_h$) and the broadness of the intensity size distribution, polydispersity index (PDI), were obtained from the intensity curve fitting by applying the autocorrelation function using an integrated Kalliope Ver. 2.16.0 software (Anton Paar GmbH).

2.2.5. Scanning Electron Microscopy (SEM)

The morphology of the particles was characterized by GeminiSEM 500 (Carl-Zeiss Microscopy GmbH, Jena, Germany) at an acceleration voltage of 1 kV. A total of 0.01–0.1 mg/mL of samples were taken in a Hamilton syringe and applied on the $CO_2$ snow jet-cleaned silicon plate at a volume of 5 to 10 µL followed by air-drying. The average particle size of each sample was determined by fitting the size distribution histogram to the log-normal distribution function.

2.2.6. Synthesis of Stearate-Hydroxyethyl Starch (St-HES) Conjugates

The synthesis of modified HES was carried out via a simple Steglich esterification reaction [26,29] with small modifications. Briefly, 1 g (5.45 mmol) of HES was dried at 110 °C for 2 h before dissolving in 20 mL of anhydrous DMF in a round bottom flask. Either 0.52 g (1.83 mmol) or 1.03 g (3.63 mmol) of SA were added to that solution and left under stirring with a speed of 400 rpm at 40 °C until it turned into a clear solution. Afterwards, EDC·HCl (3 eq.) and DMAP (0.3 eq.) were added to the solution and the flask was tightly sealed and stirred for 24 h at 40 °C. Then, the reactant mixture was cooled down to room temperature and precipitated in an ethanol:diethyl ether (1:1) solvent mixture and kept at 4 °C until the precipitate completely settled down. The solvent was decanted, and the procedure was repeated three times with the same solvent mixture. Finally, the precipitate was dialyzed against distilled water for three days and then lyophilized.

2.2.7. Preparation of Self-Assembled Nanoparticles of St-HES Conjugates

Self-assembled nanoparticles were prepared according to the nanoprecipitation method [30]. A total of 10 mg of each conjugate was dissolved in 1 mL of DMSO or THF into a small vial under magnetic stirring at 60 °C. After complete dissolution, the solution was slowly injected using a syringe pump into 10 mL of distilled water previously equilibrated at 60 °C under rapid magnetic stirring. Afterwards, the dispersion was poured into an ice-cooled empty vial under magnetic stirring to attain rapid solidification and kept stirring for 3 h to homogenize the system. Then, the dispersion was dialyzed against distilled water for three days and finally, part of the water was removed by rotary evaporator to obtain a 0.1 mg/mL dispersion.

## 3. Results and Discussion

### *3.1. Characterization of HES*

HES, a derivative of natural starch, was selected for the synthesis of highly grafted hydrophobicized HES conjugates due to its abundance of hydroxyl groups, allowing easy modifications according to the desired properties and designing programmable self-assembled nanocarriers with multiple functionalities [31]. Previously, Kulicke et al. reported the chemical characterization of HES by 1D NMR spectroscopy [32]. However, it is worthwhile to investigate a detailed 2D NMR analysis of the native HES to provide precise information regarding $^{1}$H and $^{13}$C assignments and subsequently the calculation of the degree of grafting. Thus, a comprehensive structural characterization of native HES was performed by utilizing $^{1}$H NMR including labile proton exchange phenomena, 2D HSQC, and HMBC spectroscopy. Here, the –OH substitutions by the hydroxyethyl groups and

branching points are denoted as (s) and (b), respectively. Figure 1 shows the $^{1}$H NMR spectrum of HES in DMSO-$d_6$ including the chemical structure and the signal assignments.

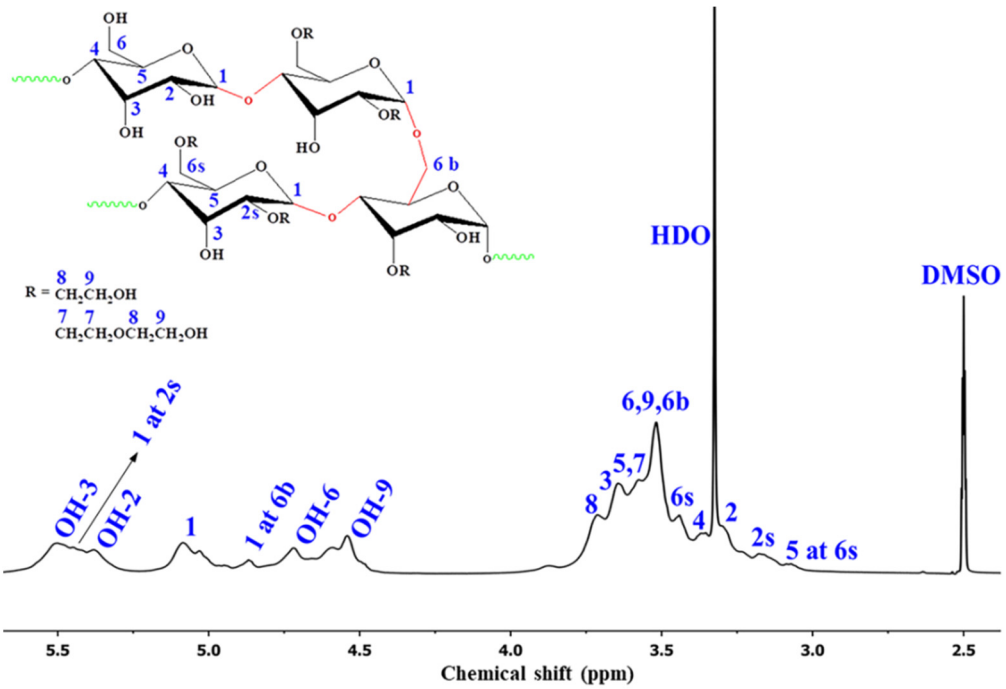


**Figure 1.** $^{1}$H NMR spectrum of HES in DMSO-$d_6$ at 27 °C. The inset shows the structure of HES with peak assignments.

In Figure 1, significant peak overlapping is observed, making it challenging to identify and assign all the peaks in the spectrum [33–36]. The anomeric proton resonances of H-1 at α-1,4 unsubstituted (peak 1), H-1 at α-1,4 substituted at C-2 position by hydroxyethyl group (peak 1 at (2s)), and H-1 at α-1,6 branching points (peak 1 at (6b)) are also difficult to resolve due to signal overlapping with the hydroxyl group (–OH) peaks from the anhydroglucose unit (AGU) of HES in the region of $\delta_H$ 4.44−5.70 ppm. To determine the peaks raised from anomeric protons, $^{1}$H NMR measurements (Figure 2) were carried out in $D_2O$ and $D_2O$/DMSO-$d_6$ mixture 1:9 ratio so that the protons of the hydroxyl groups of HES can rapidly exchange with labile deuterium.

As shown in Figure 2A,C, due to deuterium exchange only the anomeric protons are observed in the range of $\delta_H$ 4.44–5.70 ppm. By comparing Figure 2A–C, the $^{1}$H NMR chemical shift at 5.45 ppm, 5.08 ppm, and 4.86 ppm can be identified as the anomeric protons labeled as peak 1, peak 1 at (2s), and peak 1 at (6b) [32,37–41]. All other ring protons of the HES backbone coalesced into a broad peak 2–9 between $\delta_H$ 3.02 and 3.92 ppm. Based on the $^{1}$H and $^{13}$C NMR peak assignment of starch, and its derivatives, it is possible to assign the proton resonance signals raised from the AGU of HES denoted as peaks 2 to 9 in the region of $\delta_H$ 3.02–3.92 [32,37–39,41,42]. For complete characterization of the native HES, 2D NMR experiments, namely $^{1}$H-$^{13}$C HSQC and $^{1}$H-$^{13}$C HMBC spectroscopy were performed. Figure 3 represents the HSQC and HMBC NMR spectra of HES. The $^{1}$H and the APT $^{13}$C spectra are depicted on the x- and y-axis, respectively. In Figure 3A the HSQC NMR spectrum, the correlation signals of AGU at $\delta_C/\delta_H$ 100.23/5.08, 71.72/3.29, 73.28/3.64, 79.01/3.36, 71.15/3.57, 60.49/3.51, 72.40/3.57, and 72.40/3.71 correspond to C1/H1, C2/H2, C3/H3, C4/H4, C5/H5, C6/H6 and C9/H9, C7/H7, and C8/H8, respectively. In addition, other correlation signals are also observed due to branching and –OH substitution by the hydroxyethyl group. The correlation peaks at $\delta_C/\delta_H$ 80.15/3.17, 72.18/3.44, 70.13/3.06, 96.43/5.45, and 69.14/3.52 are attributed to C2s/H2s, C6s/H6s, C5 at (6s)/H5 at (6s), C1 at (2s)/H1 at (2s), and C6b/H6b, respectively.

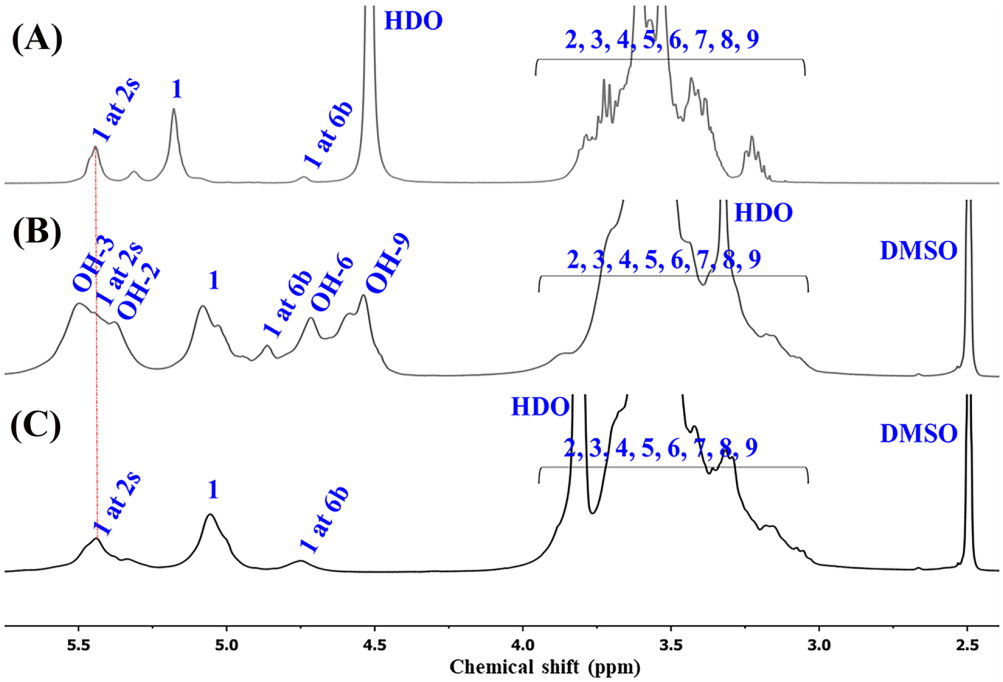


**Figure 2.** $^{1}$H NMR spectra of HES in (**A**) $D_2O$, (**B**) DMSO-$d_6$, and (**C**) $D_2O$/DMSO-$d_6$ (1:9) at 27 °C. The structure of HES is given in the inset of Figure 1.

However, the HSQC NMR spectrum depicts only the correlation signal between each carbon with its directly attached protons. Because of this phenomenon, the signal for OH-2, 3, 6, and 9 could not be detected as these protons are not directly attached to the carbon atom of the HES molecule. To identify the proton shift in the hydroxyl groups and other protons, the 2D HMBC experiment was recorded which reveals the correlation between carbon and protons in the long range ($^{2}J_{C\text{-}H}$ or more). Figure 3B represents the HMBC spectrum of HES. In Figure 3B, the correlation signals at $\delta_C/\delta_H$ 60.49/4.72, 70.13/4.86, 73.28/4.86, 71.15/4.72, 60.49/4.54, 72.40/4.54, 60.49/3.71, 80.15/3.71, 60.49/3.57, 72.40/3.51, 60.49/3.44, and 70.13/3.44 correspond to C6/OH-6, C5 at (6s)/H1 at (6b), C3/H1 at (6b), C5/OH-6, C9/OH-9, C8/OH-9, C6/H8, C2s/H8, C6/H5, C8/H9, C9/H6s, and C5 at (6s)/H6s, respectively. By combining HSQC and HMBC spectra, all the resonance signals that arise from the HES backbone are readily assigned except OH-2 and OH-3. However, the $^{1}$H chemical shift of OH-2 and OH-3 can be assigned at 5.40 ppm and 5.50 ppm, respectively, based on other reports [38,39,43,44].

### *3.2. Synthesis and NMR Characterization of St-HES Conjugates*

St-HES conjugates were synthesized by the formation of ester linkage via a simple esterification reaction between the carboxylic group of SA and the hydroxyl groups of HES. The synthesis scheme of the St-HES conjugates is shown in Scheme 1.

Two different highly grafted hydrophobicized St-HES conjugates were synthesized by controlling the grafting ratio of SA to HES. The two conjugates were defined as St-HES with degrees of grafting at 29.4% (St-HES29.4) and 60.3% (St-HES60.3). The structure of St-HES conjugates was verified by $^{1}$H, 2D HSQC, and HMBC NMR spectroscopy. The $^{1}$H NMR spectra of St-HES29.4, St-HES60.3, and SA are shown in Figure 4A–C. By comparing Figures 1 and 4A–C, it is noticeable that the proton signals arising from the grafted stearate side chain are completely distinguishable from the polymer backbone. The characteristic proton signals of HES were observed between 3.01 ppm and 5.70 ppm. After modification, the new peak b at 0.80 ppm appeared, which corresponds to the methyl protons of the esterified stearate side chain. Two $^{1}$H NMR signals are observed at 1.08–1.28 ppm (peak c, d, and e) and the 1.46 ppm (peak f) is attributed to the methylene protons of stearate. The

methylene protons attached to the carbonyl group of the ester linkage give a resonance signal at 2.24 ppm (peak g) [26].

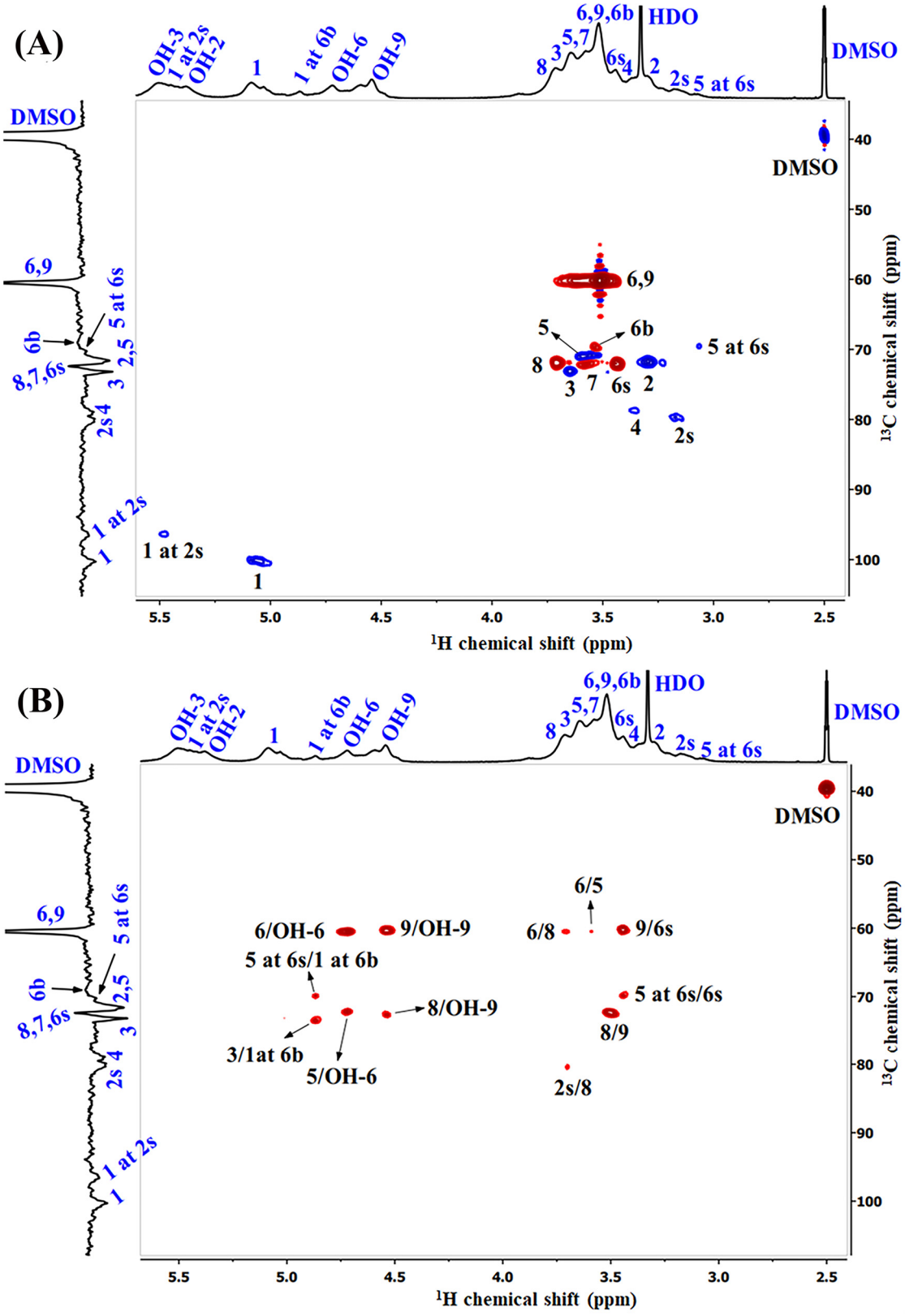


**Figure 3.** (**A**) HSQC and (**B**) HMBC NMR spectra of HES in DMSO-$d_6$ at 27 °C. The structure of HES is given in the inset of Figure 1.

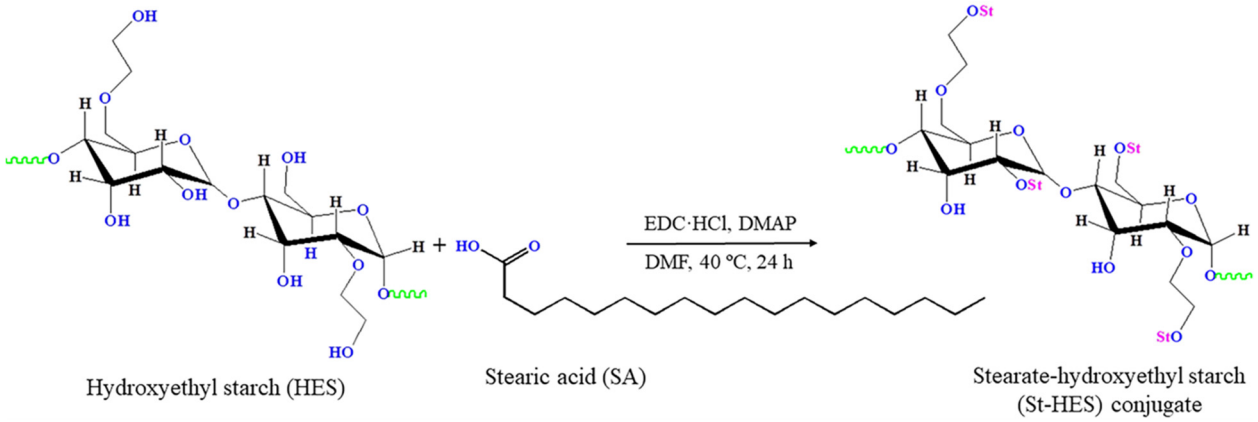


**Scheme 1.** Synthetic pathway for stearate-hydroxyethyl starch (St-HES) conjugates.

The complete disappearance of the proton signal of the carboxyl group of SA at 11.93 ppm, is an indication of HES conjugation with SA. The chemical structure of St-HES conjugates was further characterized by HSQC and HMBC NMR spectroscopy. As both St-HES29.4 and St-HES60.3 have similar structures except for variation in the degree of grafting, only the 2D NMR spectra for St-HES29.4 are shown in Figure 5. The $^{1}$H and $^{13}$C spectra are presented along the x- and y-axis, respectively. In Figure 5A the HSQC NMR spectrum, a cross-peak at $\delta_C/\delta_H$ 13.81/0.80 belongs to the Cb/Hb signal, which represents the methyl group of stearates. The correlation signals at 22.02/1.08–1.28, 31.32/1.08–1.28, and 29.09/1.08–1.28 are attributed to the methylene groups of grafted chain denoted as Cc/Hc, Cd/Hd, and Ce/He. The cross-peak Cf/Hf ($\delta_C/\delta_H$ 24.41/1.46) is related to the methylene group adjacent to the carbonyl group and the cross-peak Cg/Hg ($\delta_C/\delta_H$ 33.45/2.24) is assigned as the methylene group directly attached to the carbonyl group. Figure 5B represents the HMBC spectrum of St-HES29.4. The correlation signals at $\delta_C/\delta_H$ 22.02/0.80, 31.32/0.80, 22.02/1.08–1.28, 29.09/1.08–1.28, and 31.32/1.08–1.28 are attributed to the Cc/Hb, Cd/Hb, Cc/Hd, Ce/Hd, and Cd/Hf or He, respectively. A new $^{13}$C chemical shift is observed at 175.16 ppm, with no corresponding cross-peak in the HSQC and HMBC NMR spectra (Figure 5A,B) assigned as the carbonyl signal from the newly formed ester linkage (–COO). This is a clear indication of the efficient conjugation of St-HES. The degree of grafting is defined as the number of stearate chains attached to 100 AGUs. The degree of grafting is determined as 29.4% (St-HES29.4) and 60.3% (St-HES60.3) from the integration peak a and peak b shown in the $^{1}$H NMR spectra (Figure 4A,B), using Equation (1).

$$Degree\ of\ grafting = \left( \frac{\frac{I_b}{3}}{\frac{I_a + \frac{I_b}{3}}{4}} \right) \quad (1)$$

Here, $I_b$ is the integral value of three methyl protons from the stearate side chains and $I_a$ is the integral of the four protons, particularly the anomeric proton and the three protons from the hydroxyl groups of the AGU.

### *3.3. DSC and WAXS Analysis*

The thermal and crystalline behavior of native HES, St-HES29.4, and St-HES60.3 were investigated by DSC and WAXS, respectively (Figure 6). Figure 6A represents the DSC thermograms of HES, St-HES29.4, and St-HES60.3 in the temperature range between −60 °C and 120 °C at a heating rate of 1 K/min. All the DSC thermograms shown here are taken from the second heating curve. The DSC curve (Figure 6A) of native HES shows that this polymer is fully amorphous in the temperature range studied. Consequently, the DSC thermogram of St-HES29.4, containing 29.4% stearate side chains, does not show any melting endotherm and behaves like an amorphous polymer. This demonstrates that the grafted stearate chains on HES form non-crystalline structures with no distinct

ordered arrangement of the chains. One reason is that the amorphous HES prevents the crystallization of side chains, thus no characteristic endothermal peak is observed during the heating cycle [45]. With increasing the grafting ratio from 29.4% (St-HES29.4) to 60.3% (St-HES60.3), a melting transition appeared in the DSC thermogram (Figure 6A). Since HES is an amorphous polymer, the endothermal transition arises from the stearate side chains, which indicates a semi-crystalline behavior of St-HES60.3 [46]. This can be explained by the differences in the grafting ratio of St-HES29.4 and St-HES60.3. When the grafting ratio increased from 29.4% to 60.3%, the stearate chains on the HES backbone were sufficient to form a regular arrangement of the side chains and pack into an ordered crystal structure [47]. St-HES60.3 shows a broad melting range of −7 °C to 29 °C, with a melting point ($T_m$) of 21.2 °C taken as the maximum of the DSC heating curve (Figure 6A). In addition, the DSC thermogram of St-HES60.3 shows that grafting SA with amorphous HES at around 60% causes the melting point depression of SA ($T_m$ of SA is 69.3 °C [48]) and is close to the $T_m$ of octadecane (28–30 °C) [46]. One possible explanation could be that the amorphous nature of HES and the random distribution of the stearate chains along the HES backbone might interfere with the highly ordered packing of the side chains, resulting in the formation of more imperfect crystals of varying sizes [49,50]. These results further confirmed that HES was successfully grafted with SA.

The WAXS patterns of SA, HES, St-HES29.4, and St-HES60.3 are presented in Figure 6B and were recorded (except SA measured at room temperature) at −30 °C. The Bragg reflections from the silicon substrate appeared below 2θ = 8° and at more than 30°. Hence, no interference was observed with the measured samples. SA exhibits sharp diffraction peaks at 2θ of 19.18°, 21.74°, and 24.43°, shown in Figure 6B, demonstrating the crystalline nature of SA at room temperature. The pure HES showed a broad amorphous halo in the range of 2θ = 13°–27° indicating that the sample is completely amorphous [51]. Furthermore, the WAXS profile of St-HES29.4 did not show any distinct Bragg reflections rather than a big halo, which is consistent with the DSC result. The absence of characteristic diffraction peaks of pure SA in the grafted St-HES29.4 indicates the complete disappearance of the crystalline nature of SA after conjugation. However, St-HES60.3 showed a strong reflection at 2θ = 21.84° together with an amorphous halo, which is in agreement with the DSC analysis (Figure 6A). This diffraction peak may be attributed to the intense Bragg reflection raised from the 110 plane of SA, which usually appeared at 2θ = 21.74° (Figure 6B) in pure SA. This result suggests that the partial crystalline nature of St-HES60.3 arises only from the grafted side chains.

### *3.4. Characterization of Self-Aggregated St-HES Conjugates*

The St-HES conjugates could readily self-assemble in aqueous media and form micelles or self-aggregates due to intra- or intermolecular hydrophobic interactions [9]. The hydrophilic backbone of HES forms the outer shell of the micelles, and the hydrophobic stearate segments are oriented towards the core to achieve an energy-minimized spherical structure [52,53]. Figure 7 shows the size distribution of self-aggregates of St-HES29.4 and St-HES60.3 conjugates in distilled water as determined by DLS. In Figure 7A, the intensity size distribution of the St-HES29.4 conjugate shows a monomodal size distribution with a hydrodynamic diameter ($D_h$) of 130.7 nm and a polydispersity index (PDI) of 0.16. A similar self-assembled behavior was observed for the St-HES60.3 conjugate. The DLS histogram of the St-HES60.3 conjugate (Figure 7B) suggests a single Gaussian distribution (monomodal) of the sample with a $D_h$ of 152.5 nm and a PDI of 0.21. The size of St-HES micelles increases from 130.7 nm to 152.5 nm, with an increase in the grafting ratio of stearate side chains from 29.4% (St-HES29.4) to 60.3% (St-HES60.3) possibly due to two factors. Firstly, two different solvents, DMSO for St-HES29.4 and THF for St-HES60.3, were used initially to dissolve the conjugates to formulate micelles in water, which could impact the average particle dimensions later [54]. Secondly, the higher degree of side chain grafting would lead to aggregating more St-HES chains close together in one particle. Consequently, more chain aggregation in one particle results in more repulsive forces between and within the hydrophobic stearate chains, which in turn contributes to the overall increase in particle size [8].

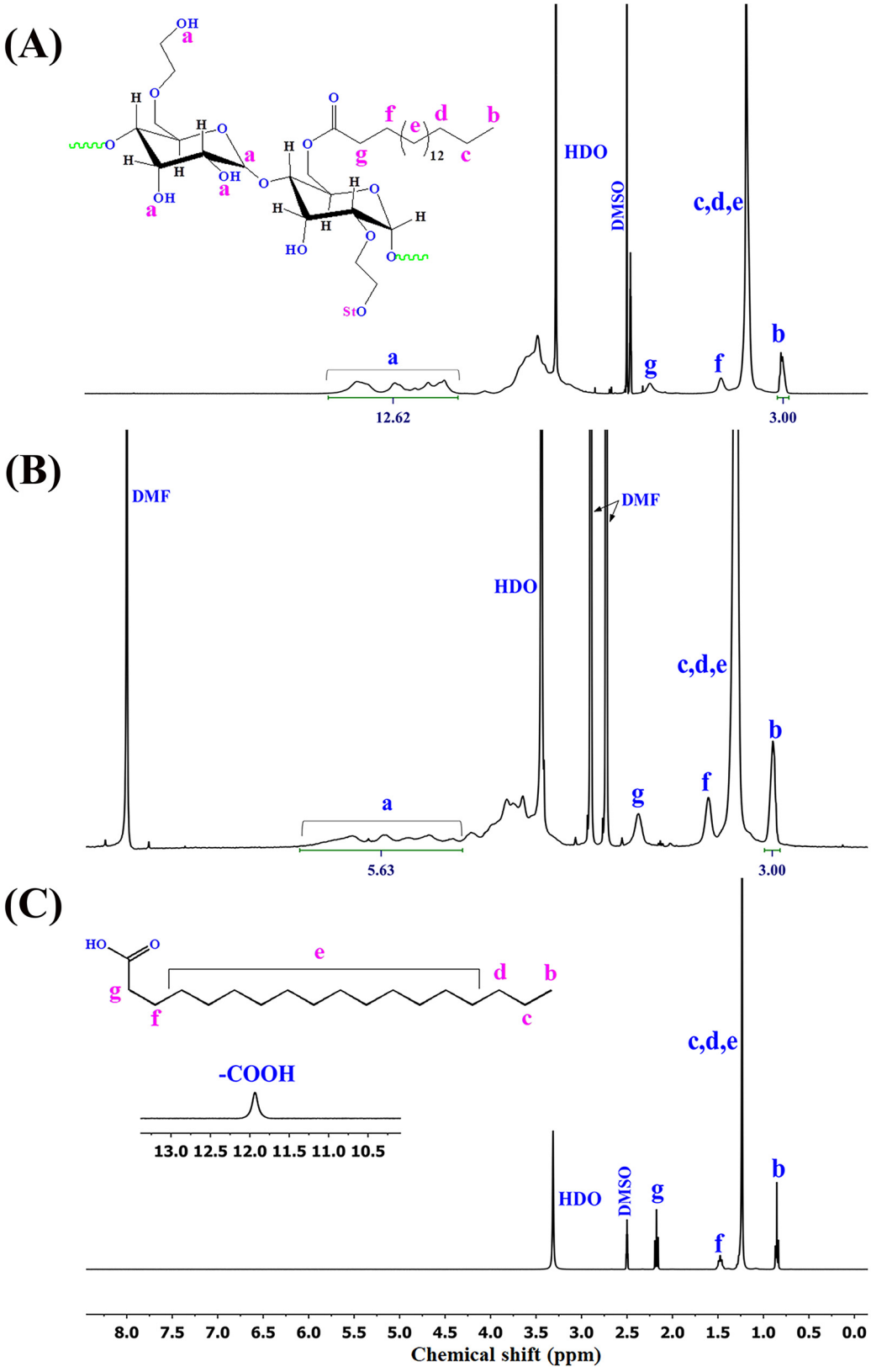


**Figure 4.** The $^{1}$H NMR spectra of (**A**) St-HES29.4 and (**B**) St-HES60.3 were recorded at 50 °C using DMSO-$d_6$ and DMF-$d_7$ as solvents, respectively. The (**C**) $^{1}$H NMR spectrum of SA was recorded at 27 °C using DMSO-$d_6$.

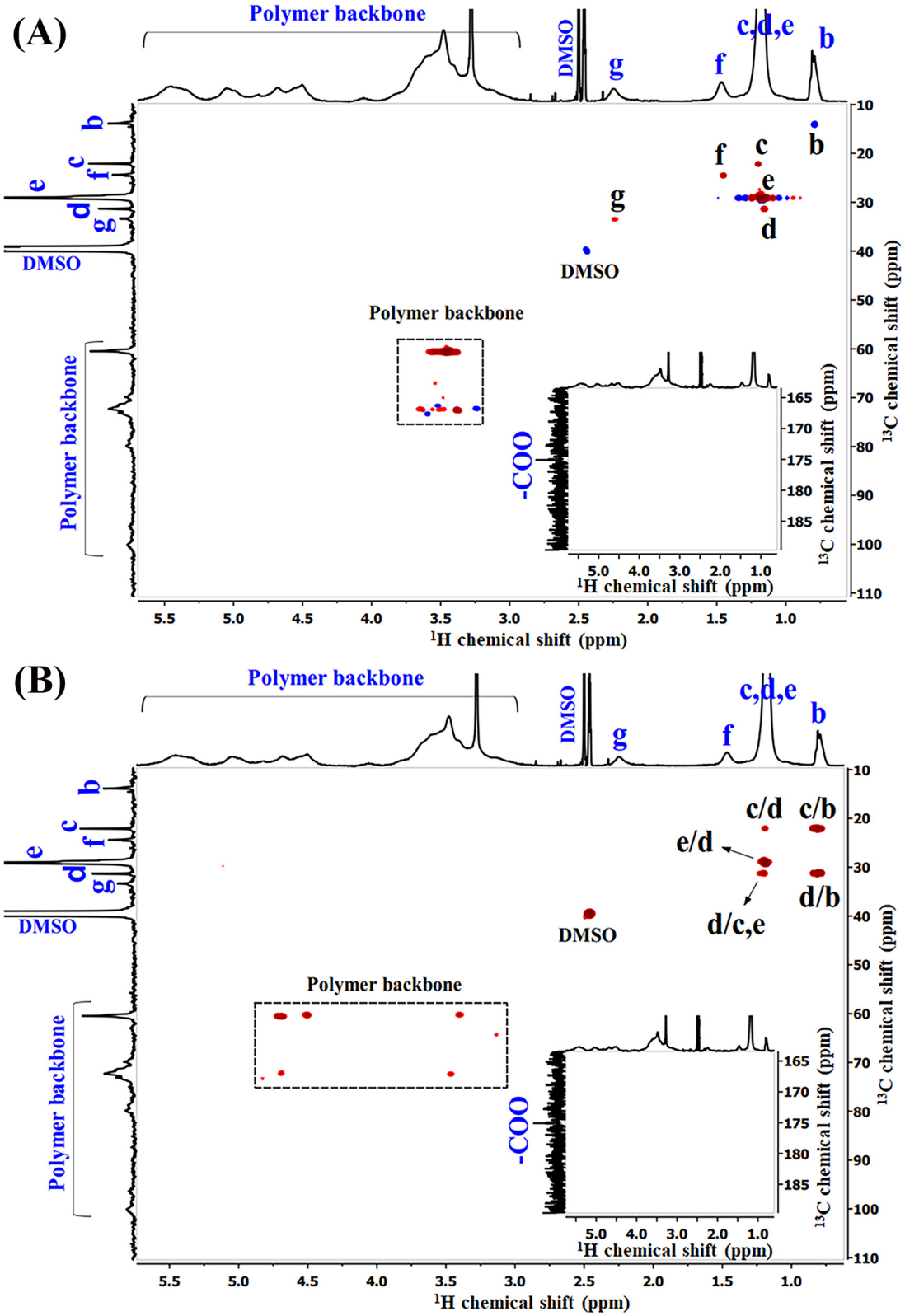


**Figure 5.** (**A**) HSQC and (**B**) HMBC NMR spectra of St-HES29.4 in DMSO-$d_6$ at 50 °C. The structure of St-HES is given in the inset of Figure 4(**A**). The insets show the range of 1−5.5 ppm and 165−185 ppm for $^{1}$H and $^{13}$C NMR chemical shifts, respectively. No additional correlation signals are observed for –COO.

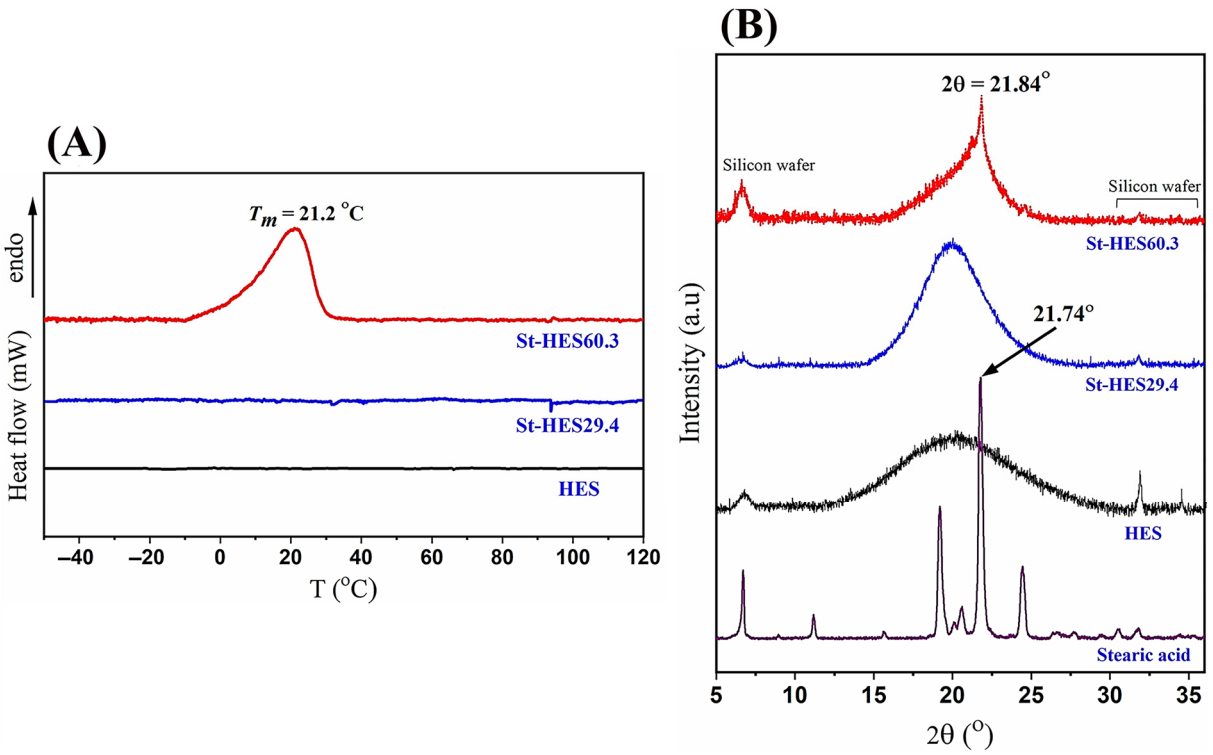


**Figure 6.** (**A**) DSC traces of HES, St-HES29.4, and St-HES60.3, with the respective melting temperature, $T_m$, recorded at a heating rate of 1 K/min. (**B**) WAXS diffraction patterns of SA, HES, St-HES29.4, and St-HES60.3 at T = −30 °C (except SA measured at room temperature).

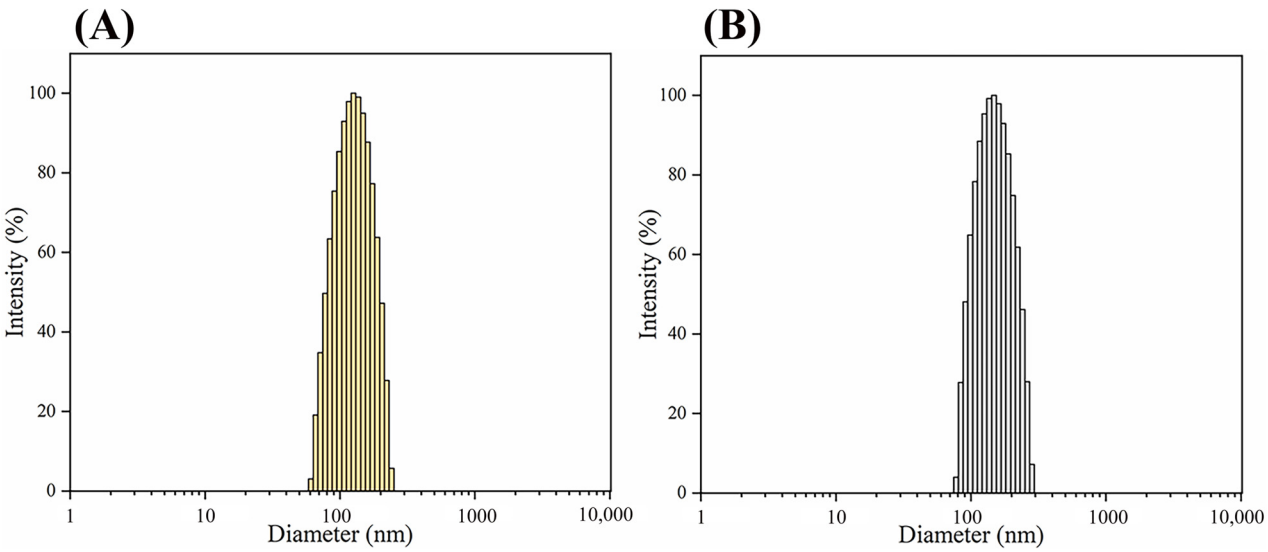


**Figure 7.** Intensity-weighted particle size distribution of (**A**) St-HES29.4 and (**B**) St-HES60.3 in distilled water measured by DLS at 25 °C.

To further examine the morphology of St-HES micelles, SEM was carried out by dispersing the prepared samples and drying them on the silicon substrate. Figure 8A–D represent the SEM images and size distribution of St-HES29.4 and St-HES60.3, respectively. The SEM microphages demonstrate that both samples are nearly spherical in shape and, to some extent, collapse structures are formed, as shown in Figure 8A–C.

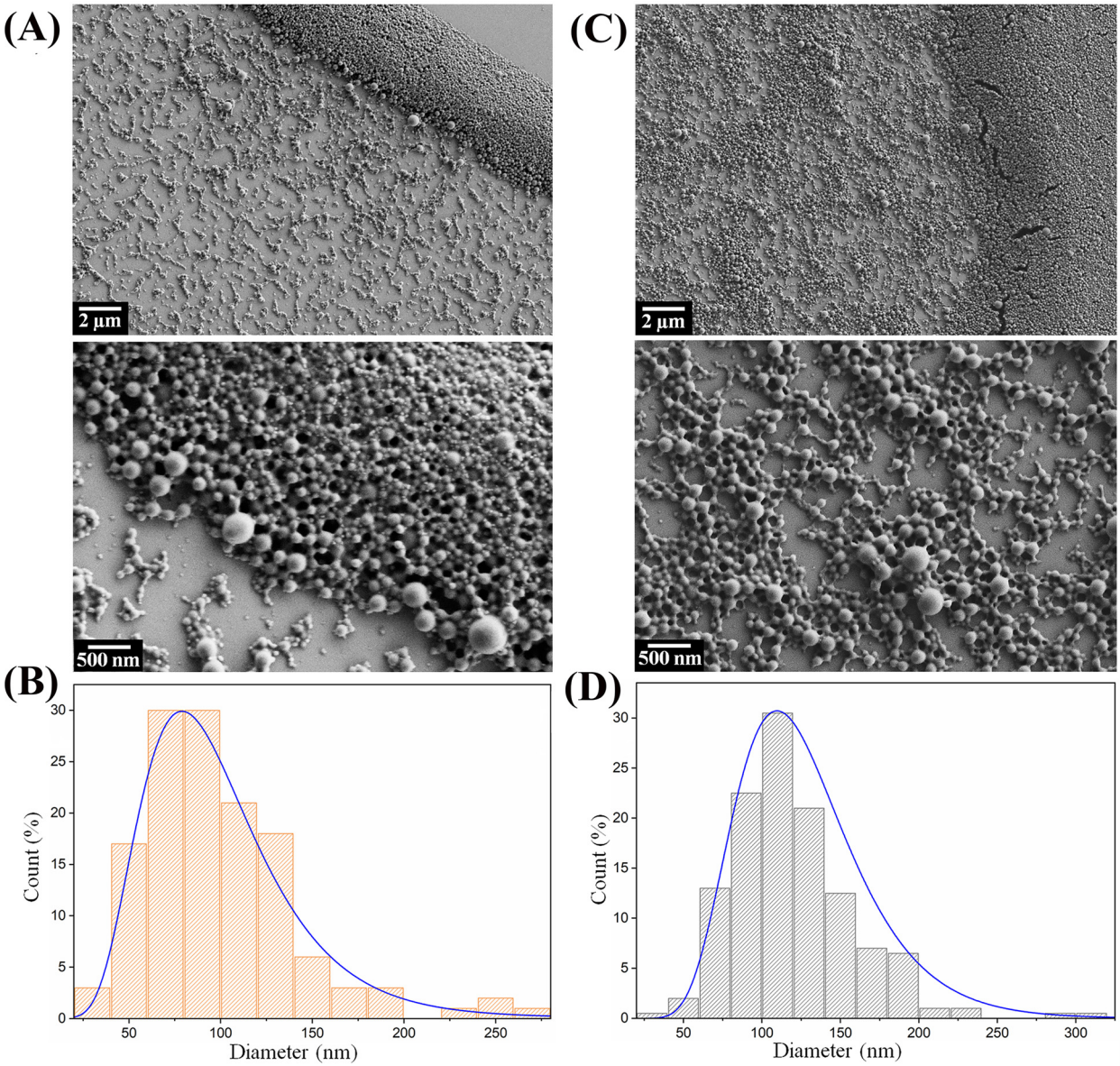


**Figure 8.** SEM images of (**A**) St-HES29.4 (left) and (**C**) St-HES60.3 (right) nanoparticles with the respective particle size distribution (**B**,**D**) obtained by fitting with a log-normal distribution function.

The mean diameter of St-HES29.4 and St-HES60.3 was 99.8 nm (Figure 8B) and 119.4 nm (Figure 8D), respectively, estimated by fitting the particle size distribution curve obtained from SEM images. However, the size of the micelles measured by SEM appeared to be smaller than the results obtained by DLS analysis. This may be due to the different states of the samples during measurements. The DLS method provides the size as $D_h$ of the particles in the hydrated state, while SEM images are obtained from the dried state of the samples. Hence, during SEM sample preparation, the drying process induces particle collapse and causes shrinkage of the aggregates, leading to the formation of smaller particles than those obtained by the DLS method [55]. It is also noticeable that the size of the micelles increased when increasing the grafting ratio of St-HES from 29.4% to 60.3%, which is in good agreement with the DLS measurements.

## 4. Conclusions

In conclusion, the synthesis of stearate-substituted esters of HES is reported to obtain highly hydrophobic St-HES conjugates, St-HES29.4 and St-HES60.3. The structural and

physicochemical properties of the synthesized conjugates were investigated by NMR, DSC, and WAXS experiments. The $^{1}$H and 2D NMR spectra of the St-HES conjugates revealed the successful conjugation via ester bond formation. In addition, thermal analyses and WAXS experiments showed a complete transition from fully amorphous HES to semicrystalline St-HES60.3. Both conjugates, St-HES29.4 and St-HES60.3, self-assembled in water and provided a monodispersive particle size distribution with a $D_h$ of 130.7 nm and 152.5 nm, respectively. The SEM images of the self-aggregates showed the formation of nearly spherical particles. The mean diameter appeared to be smaller than obtained by DLS measurements due to the drying procedure of the SEM samples. However, the dependence of particle size on the grafting ratio was in good agreement with DLS. The synthesized nano-assembly could potentially be applied in the pharmaceutical field, i.e., to encapsulate poorly water-soluble drugs with a high-loading capacity and prolong the drug circulation time and oral delivery of labile bioactive agents to optimize drug stability in the gastrointestinal tract with improved absorption and complexation with protein therapeutics to resist denaturation and enhance thermal stability.

In addition, a complete structural characterization of native HES was analyzed utilizing labile proton exchange phenomena of the hydroxyl groups to determine the anomeric proton signals in $^{1}$H NMR spectra. Furthermore, 2D NMR spectroscopy was performed to determine the other proton signals raised from the HES backbone and to verify the structure more precisely. Finally, it is demonstrated that 1D and 2D NMR spectroscopy provide a more detailed and clear structural analysis of HES and an exact determination of the degree of grafting of St-HES conjugates.

**Author Contributions:** Conceptualization, R.H. and J.K.; methodology, R.H. and J.K.; investigation, R.H., H.R., and F.S.; writing—original draft preparation, R.H.; writing—review and editing, R.H. and J.K.; supervision, J.K.; funding acquisition, J.K. All authors have read and agreed to the published version of the manuscript.

**Funding:** This work was conducted in the frame of the International Graduate School AGRIPOLY, supported by the European Social Fund (ESF) and the Federal State Saxony-Anhalt.

**Institutional Review Board Statement:** Not applicable.

**Informed Consent Statement:** Not applicable.

**Data Availability Statement:** The data presented in this article are available upon request. Samples of the compounds are available upon request from the authors.

**Acknowledgments:** We would like to thank Dieter Ströhl and Nazmul Hasan for their help during the NMR and WAXS measurements.

**Conflicts of Interest:** The authors declare no conflicts of interest.

## References

1. Kashapov, R.; Gaynanova, G.; Gabdrakhmanov, D.; Kuznetsov, D.; Pavlov, R.; Petrov, K.; Zakharova, L.; Sinyashin, O. Self-Assembly of Amphiphilic Compounds as a Versatile Tool for Construction of Nanoscale Drug Carriers. *Int. J. Mol. Sci.* **2020**, *21*, 6961. [CrossRef]
2. Yang, J.; Gao, C.; Lü, S.; Zhang, X.; Yu, C.; Liu, M. Physicochemical Characterization of Amphiphilic Nanoparticles Based on the Novel Starch-Deoxycholic Acid Conjugates and Self-Aggregates. *Carbohydr. Polym.* **2014**, *102*, 838–845. [CrossRef]
3. Jones, M.C.; Leroux, J.C. Polymeric Micelles—A New Generation of Colloidal Drug Carriers. *Eur. J. Pharm. Biopharm.* **1999**, *48*, 101–111. [CrossRef]
4. Kesharwani, R.; Tripathy, S.; Patel, D.K.; Yadav, P.K.; Das, M.K. Multifunctional Micellar Nanomedicine for Cancer Therapy. *Multifunct. Theranostic Nanomed. Cancer* **2021**, *234*, 57–65.
5. Francis, M.F.; Cristea, M.; Winnik, F.M. Polymeric Micelles for Oral Drug Delivery: Why and How. *Pure Appl. Chem.* **2004**, *76*, 1321–1335. [CrossRef]
6. Li, Y.; Xiao, K.; Luo, J.; Xiao, W.; Lee, J.S.; Gonik, A.M.; Kato, J.; Dong, T.A.; Lam, K.S. Well-Defined, Reversible Disulfide Cross-Linked Micelles for on-Demand Paclitaxel Delivery. *Biomaterials* **2011**, *32*, 6633–6645. [CrossRef] [PubMed]
7. Lu, Y.; Zhang, E.; Yang, J.; Cao, Z. Strategies to Improve Micelle Stability for Drug Delivery. *Nano Res.* **2018**, *11*, 4985–4998. [CrossRef]

8. Zhou, H.; Yu, W.; Guo, X.; Liu, X.; Li, N.; Zhang, Y.; Ma, X. Synthesis and Characterization of Amphiphilic Glycidol-Chitosan-Deoxycholic Acid Nanoparticles as a Drug Carrier for Doxorubicin. *Biomacromolecules* **2010**, *11*, 3480–3486. [CrossRef]
9. Yadav, S.; Sharma, A.K.; Kumar, P. Nanoscale Self-Assembly for Therapeutic Delivery. *Front. Bioeng. Biotechnol.* **2020**, *8*, 127. [CrossRef]
10. Li, Y.; Gao, Q. Novel Self-Assembly Nano OSA Starch Micelles Controlled by Protonation in Aqueous Media. *Carbohydr. Polym.* **2023**, *299*, 120146. [CrossRef]
11. Sun, Y.; Bai, Y.; Yang, W.; Bu, K.; Tanveer, S.K.; Hai, J. Global Trends in Natural Biopolymers in the 21st Century: A Scientometric Review. *Front. Chem.* **2022**, *10*, 915648. [CrossRef] [PubMed]
12. Liu, Z.; Jiao, Y.; Wang, Y.; Zhou, C.; Zhang, Z. Polysaccharides-Based Nanoparticles as Drug Delivery Systems. *Adv. Drug Deliv. Rev.* **2008**, *60*, 1650–1662. [CrossRef] [PubMed]
13. Liu, J.; Li, J.; Ma, Y.; Chen, F.; Zhao, G. Synthesis, Characterization, and Aqueous Self-Assembly of Octenylsuccinate Oat β-Glucan. *J. Agric. Food Chem.* **2013**, *61*, 12683–12691. [CrossRef] [PubMed]
14. Fan, Y.; Liu, Y.; Wu, Y.; Dai, F.; Yuan, M.; Wang, F.; Bai, Y.; Deng, H. Natural Polysaccharides Based Self-Assembled Nanoparticles for Biomedical Applications—A Review. *Int. J. Biol. Macromol.* **2021**, *192*, 1240–1255. [CrossRef] [PubMed]
15. Hey, T.; Helmut, K.; Vorstheim, P. Half-life Extension through HESylation®. In *Therapeutic Proteins: Strategies to Modulate Their Plasma Half-Lives*; Kontermann, R., Ed.; Wiley-VCH Verlag Gmbh & Co. KGaA: Weinheim, Germany, 2012; pp. 117–140, ISBN 9780470411964.
16. Besheer, A.; Liebner, R.; Meyer, M.; Winter, G. Challenges for PEGylated Proteins and Alternative Half-Life Extension Technologies Based on Biodegradable Polymers. *ACS Symp. Ser.* **2013**, *1135*, 215–233.
17. Wang, H.; Hu, H.; Yang, H.; Li, Z. Hydroxyethyl Starch Based Smart Nanomedicine. *RSC Adv.* **2021**, *11*, 3226–3240. [CrossRef] [PubMed]
18. Treib, J.; Baron, J.F.; Grauer, M.T.; Strauss, R.G. An International View of Hydroxyethyl Starches. *Intensive Care Med.* **1999**, *25*, 258–268. [CrossRef] [PubMed]
19. Dumitriu, S. *Polysaccharides in Medicinal Applications*; Marcel Dekker Inc.: New York, NY, USA, 1996.
20. Liebner, R.; Mathaes, R.; Meyer, M.; Hey, T.; Winter, G.; Besheer, A. Protein HESylation for Half-Life Extension: Synthesis, Characterization and Pharmacokinetics of HESylated Anakinra. *Eur. J. Pharm. Biopharm.* **2014**, *87*, 378–385. [CrossRef]
21. Besheer, A.; Hertel, T.C.; Kressler, J.; Mäder, K.; Pietzsch, M. Enzymatically Catalyzed HES Conjugation Using Microbial Transglutaminase: Proof of Feasibility. *J. Pharm. Sci.* **2009**, *98*, 4420–4428. [CrossRef]
22. Xiao, C.; Hu, H.; Yang, H.; Li, S.; Zhou, H.; Ruan, J.; Zhu, Y.; Yang, X.; Li, Z. Colloidal Hydroxyethyl Starch for Tumor-Targeted Platinum Delivery. *Nanoscale Adv.* **2019**, *1*, 1002–1012. [CrossRef]
23. Paleos, C.M.; Sideratou, Z.; Tsiourvas, D. Drug Delivery Systems Based on Hydroxyethyl Starch. *Bioconjug. Chem.* **2017**, *28*, 1611–1624. [CrossRef] [PubMed]
24. Hore, R.; Alaneed, R.; Pietzsch, M.; Kressler, J. Enzymatic HES Conjugation with Recombinant Human Erythropoietin via Variant Microbial Transglutaminase TG$^{16}$. *Starch/Stärke* **2022**, *74*, 2200034. [CrossRef]
25. Tan, R.; Wan, Y.; Yang, X. Hydroxyethyl Starch and Its Derivatives as Nanocarriers for Delivery of Diagnostic and Therapeutic Agents towards Cancers. *Biomater. Transl.* **2020**, *1*, 46–57. [PubMed]
26. Besheer, A.; Hause, G.; Kressler, J.; Mäder, K. Hydrophobically Modified Hydroxyethyl Starch: Synthesis, Characterization, and Aqueous Self-Assembly into Nano-Sized Polymeric Micelles and Vesicles. *Biomacromolecules* **2007**, *8*, 359–367. [CrossRef] [PubMed]
27. Hu, F.Q.; Zhao, M.D.; Yuan, H.; You, J.; Du, Y.Z.; Zeng, S. A Novel Chitosan Oligosaccharide-Stearic Acid Micelles for Gene Delivery: Properties and in Vitro Transfection Studies. *Int. J. Pharm.* **2006**, *315*, 158–166. [CrossRef] [PubMed]
28. Shaki, H.; Vasheghani-Farahani, E.; Ganji, F.; Jafarzadeh-Holagh, S.; Taebnia, N.; Dolatshahi-Pirouz, A. A Self Assembled Dextran-Stearic Acid-Spermine Nanocarrier for Delivery of Rapamycin as a Hydrophobic Drug. *J. Drug Deliv. Sci. Technol.* **2021**, *66*, 102768. [CrossRef]
29. Neises, B.; Steglich, W. Simple Method for the Esterification of Carboxylic Acids. *Angew. Chem. Int. Ed. Engl.* **1978**, *17*, 522–524. [CrossRef]
30. Weiss, V.M.; Naolou, T.; Amado, E.; Busse, K.; Mäder, K.; Kressler, J. Formation of Structured Polygonal Nanoparticles by Phase-Separated Comb-like Polymers. *Macromol. Rapid Commun.* **2012**, *33*, 35–40. [CrossRef] [PubMed]
31. Labelle, M.A.; Ispas-Szabo, P.; Mateescu, M.A. Structure-Functions Relationship of Modified Starches for Pharmaceutical and Biomedical Applications. *Starch/Stärke* **2020**, *72*, 2000002. [CrossRef]
32. Kulicke, W.-M.; Roessner, D.; Kull, W. Characterization of Hydroxyethyl Starch by Polymer Analysis for Use as a Plasma Volume Expander. *Starch/Stärke* **1993**, *45*, 445–450. [CrossRef]
33. Sleightholm, R.; Yang, B.; Yu, F.; Xie, Y.; Oupický, D. Chloroquine-Modified Hydroxyethyl Starch as a Polymeric Drug for Cancer Therapy. *Biomacromolecules* **2017**, *18*, 2247–2257. [CrossRef] [PubMed]
34. Li, Y.; Hu, H.; Zhou, Q.; Ao, Y.; Xiao, C.; Wan, J.; Wan, Y.; Xu, H.; Li, Z.; Yang, X. α-Amylase- and Redox-Responsive Nanoparticles for Tumor-Targeted Drug Delivery. *ACS Appl. Mater. Interfaces* **2017**, *9*, 19215–19230. [CrossRef] [PubMed]
35. Xu, Z.; Yang, D.; Long, T.; Yuan, L.; Qiu, S.; Li, D.; Mu, C.; Ge, L. PH-Sensitive Nanoparticles Based on Amphiphilic Imidazole/Cholesterol Modified Hydroxyethyl Starch for Tumor Chemotherapy. *Carbohydr. Polym.* **2022**, *277*, 118827. [CrossRef] [PubMed]

36. Li, J.; Yang, Y.; Lu, L.; Ma, Q.; Zhang, J. Preparation, Characterization and Systemic Application of Self-Assembled Hydroxyethyl Starch Nanoparticles-Loaded Flavonoid Morin for Hyperuricemia Therapy. *Int. J. Nanomed.* **2018**, *13*, 2129–2141. [CrossRef] [PubMed]
37. Nilsson, G.S.; Bergquist, K.E.; Nilsson, U.; Gorton, L. Determination of the Degree of Branching in Normal and Amylopectin Type Potato Starch with 1H-NMR Spectroscopy: Improved Resolution and Two-Dimensional Spectroscopy. *Starch/Stärke* **1996**, *48*, 352–357. [CrossRef]
38. Gong, Q.; Wang, L.Q.; Tu, K. In Situ Polymerization of Starch with Lactic Acid in Aqueous Solution and the Microstructure Characterization. *Carbohydr. Polym.* **2006**, *64*, 501–509. [CrossRef]
39. Chi, H.; Xu, K.; Wu, X.; Chen, Q.; Xue, D.; Song, C.; Zhang, W.; Wang, P. Effect of Acetylation on the Properties of Corn Starch. *Food Chem.* **2008**, *106*, 923–928. [CrossRef]
40. Richardson, S.; Nilsson, G.S.; Bergquist, K.E.; Gorton, L.; Mischnick, P. Characterisation of the Substituent Distribution in Hydroxypropylated Potato Amylopectin Starch. *Carbohydr. Res.* **2000**, *328*, 365–373. [CrossRef] [PubMed]
41. Heins, D.; Kulicke, W.M.; Käuper, P.; Thielking, H. Characterization of Acetyl Starch by Means of NMR Spectroscopy and SEC/MALLS in Comparison with Hydroxyethyl Starch. *Starch/Stärke* **1998**, *50*, 431–437. [CrossRef]
42. Gagnaire, D.; Mancier, D.; Vincendon, M. Spectres RMN Des Polysaccharides et de Leurs Dérivés: Influence Des Substituants Sur Le Déplacement Chimique 13C. *Org. Magn. Reson.* **1978**, *11*, 344–349. [CrossRef]
43. Peng, Q.J.; Perlin, A.S. Observations on N.M.R. Spectra of Starches in Dimethyl Sulfoxide, Iodine-Complexing, and Solvation in Water-Di-Methyl Sulfoxide. *Carbohydr. Res.* **1987**, *160*, 57–72. [CrossRef]
44. Liu, J.; Wang, X.; Bai, R.; Zhang, N.; Kan, J.; Jin, C. Synthesis, Characterization, and Antioxidant Activity of Caffeic-Acid-Grafted Corn Starch. *Starch/Stärke* **2018**, *70*, 1700141. [CrossRef]
45. Luo, Q.; Wang, P.; Miao, Y.; He, H.; Tang, X. A Novel 5-Fluorouracil Prodrug Using Hydroxyethyl Starch as a Macromolecular Carrier for Sustained Release. *Carbohydr. Polym.* **2012**, *87*, 2642–2647. [CrossRef]
46. Aburto, J.; Alric, I.; Thiebaud, S.; Borredon, E.; Bikiaris, D.; Prinos, J.; Panayiotou, C. Synthesis, Characterization, and Biodegradability of Fatty-Acid Esters of Amylose and Starch. *J. Appl. Polym. Sci.* **1999**, *74*, 1440–1451. [CrossRef]
47. Huang, F.Y. Thermal Properties and Thermal Degradation of Cellulose Tri-Stearate (CTs). *Polymers* **2012**, *4*, 1012–1024. [CrossRef]
48. Lide, D.R. *CRC Handbook of Chemistry and Physics*; CRC Press: Boca Raton, FL, USA, 2005.
49. Feng, L.; Kama, M.R. Distributions of Crystal Size from DSC Melting Traces for Polyethylenes. *Can. J. Chem. Eng.* **2004**, *82*, 1239–1251. [CrossRef]
50. Rim, P.B.; Runt, J.P. Melting Point Depression in Crystalline/Compatible Polymer Blends. *Macromolecules* **1984**, *17*, 1520–1526. [CrossRef]
51. Nanaki, S.G.; Koutsidis, I.A.; Koutri, I.; Karavas, E.; Bikiaris, D. Miscibility Study of Chitosan/2-Hydroxyethyl Starch Blends and Evaluation of Their Effectiveness as Drug Sustained Release Hydrogels. *Carbohydr. Polym.* **2012**, *87*, 1286–1294. [CrossRef]
52. Tuncel, D.; Demir, H.V. Conjugated Polymer Nanoparticles. *Nanoscale* **2010**, *2*, 484–494. [CrossRef]
53. Lee, K.Y.; Jo, W.H.; Kwon, I.C.; Kim, Y.H.; Jeong, S.Y. Physicochemical Characteristics of Self-Aggregates of Hydrophobically Modified Chitosans. *Langmuir* **1998**, *14*, 2329–2332. [CrossRef]
54. Gökçe Kocabay, Ö.; İsmail, O. Preparation and Optimization of Biodegradable Self-Assembled PCL-PEG-PCL Nano-Sized Micelles for Drug Delivery Systems. *Int. J. Polym. Mater. Polym. Biomater.* **2021**, *70*, 328–337. [CrossRef]
55. Golding, C.G.; Lamboo, L.L.; Beniac, D.R.; Booth, T.F. The Scanning Electron Microscope in Microbiology and Diagnosis of Infectious Disease. *Sci. Rep.* **2016**, *6*, 26516. [CrossRef] [PubMed]